Physica B 740 (2026) 419132

Contents lists available at ScienceDirect

Physica B: Condensed Matter

journal homepage: www.elsevier.com/locate/physb

An integrated AIMD and DFT study of the structural, mechanical, optoelectronic, and thermodynamic performance in $BaHfS_3$ chalcogenide perovskite

Nawzad A. Abdulkareem [a], Hameed T. Abdulla [a,*], Diyar Sadiq [b], Mohammed Noor S. Rammoo [a], Harun Akkus [c], Mehmet Erzen [c]

[a] Dep. of Physics, College of Science, University of Zakho, Theoretical Lab. of Physics, Duhok Road, Zakho, 42002, Republic of Iraq
[b] Scientific Research Centre, Duhok Polytechnic University, 61 Zakho Road, Duhok, Republic of Iraq
[c] Department of Physics, Faculty of Science, Van Yüzüncü Yıl University, Van, 65080, Turkey

ARTICLE INFO

Keywords:
$BaHfS_3$
Perovskite
DFT
AIMD
Electronic structure
Optical properties
Thermoelectric performance
BTT
Elastic anisotropy
DOS
Chalcogenide semiconductors

ABSTRACT

Chalcogenide perovskites have attracted significant attention for thermoelectric and optoelectronic applications due to their tunable electronic structures, chemical stability, and strong light–matter interactions. In this work, a comprehensive first-principles investigation of cubic $BaHfS_3$ is performed using density functional theory (DFT), density functional perturbation theory (DFPT), Boltzmann transport theory (BTT), and *ab initio* molecular dynamics (AIMD). The optimized structure stabilizes in the $Pm-3m$ phase, with a tolerance factor of 0.93 and a negative formation energy (E_f), indicating thermodynamic stability. Electronic calculations reveal an indirect band gap of 0.7 eV, dominated by *S-2p* states in the valence band and *Hf-4d* states in the conduction band. Optical analysis shows strong absorption in the visible and ultraviolet regions, along with a high static dielectric constant, supporting its suitability for optoelectronic applications. Thermoelectric results indicate a positive Seebeck coefficient, temperature-enhanced electrical conductivity, and intrinsic p-type behaviours. AIMD simulations further confirm the thermal and dynamical stability of the material, highlighting $BaHfS_3$ as a promising candidate for advanced optoelectronic and thermoelectric applications.

1. Introduction

Perovskite materials have emerged as a highly valuable family of compounds in contemporary materials science, owing to their exceptional structural flexibility and adjustable physical properties. Their general formula, ABX_3, allows for various elemental substitutions at both the A- and B-sites, facilitating extensive control over electrical, optical, and mechanical properties [1–3]. This adaptability has prompted significant investigation into perovskites for use in optoelectronics, PVs, thermoelectric, and photocatalysis. Although halide perovskites have led PV research as a consequence of their superior light-harvesting capabilities, apprehensions about toxicity and environmental stability have prompted increased interest in chalcogenide perovskite structure. These materials, comprising S- and Se-based systems, show appropriate band gaps, elevated absorption coefficients, and enhanced chemical and thermal stability, establishing them as possible candidates for next-generation optoelectronic devices [4–6]. $BaHfS_3$ is a potential chalcogenide perovskite that merges the structural integrity of barium-based compounds with the functional variety of transition metal sulfides. Research on similar compounds, including $CaZrS_3$ and $BaZrS_3$, has revealed direct or indirect semiconducting properties, substantial optical absorption in the visible spectrum, and useful thermoelectric performance [7,8]. Notwithstanding these advancements, the inherent properties of $BaHfS_3$, predominantly its structural, electrical, optical, and thermoelectric attributes under practical finite-temperature circumstances, remain insufficiently investigated.

DFT has become an integral tool for predicting intrinsic material properties, including lattice stability, electronic band structures, density of states (DOS), and optical responses [9–11]. Furthermore, the incorporation of AIMD facilitates the assessment of thermodynamic stability and a harmonic lattice effect at elevated temperatures, which are crucial for evaluating materials under device-relevant circumstances [12–14].

* Corresponding author.
E-mail addresses: nawzad.abdulkareem@uoz.edu.krd (N.A. Abdulkareem), hameed.abdulla@uoz.edu.krd (H.T. Abdulla), diyar.sadiq@dpu.edu.krd (D. Sadiq), mohammed.noor@uoz.edu.krd (M.N.S. Rammoo), harunakkus@yyu.edu.tr (H. Akkus), mehmeterzen@yyu.edu.tr (M. Erzen).

https://doi.org/10.1016/j.physb.2026.419132
Received 11 February 2026; Received in revised form 17 May 2026; Accepted 24 July 2026
Available online 25 July 2026
0921-4526/© 2026 Elsevier B.V. All rights are reserved, including those for text and data mining, AI training, and similar technologies.

On the other hand, current research on $BaHfS_3$ and other compounds is predominantly confined to 0 K static computations, resulting in a significant deficiency in comprehending the interplay between structural, electronic, and optical features with finite-temperature thermodynamic stability and thermoelectric performance.

This study employs a combined DFT and AIMD methodology to carefully assess the structural, elastic, electrical, optical, and thermoelectric properties of $BaHfS_3$. This research work advances the fundamental comprehension of this chalcogenide perovskite and evaluates its applicability for practical uses in PVs, optoelectronics, and thermoelectric energy conversion. Recent advancements in computational materials science have facilitated comprehensive investigations of the structural, mechanical, optoelectronic, and thermodynamic characteristics of many perovskite structures. Khattak et al. [15] reported that $BaXF_3$ (X = Co, Ir) fluoro-perovskites are structurally and mechanically stable, exhibiting metallic manners and promising thermoelectric features. Similarly, Xia et al. [16] demonstrated that $BaMF_3$ (M = Ag, Cu) compounds display mechanical robustness and narrow band gaps, making them suitable for high-frequency UV devices as well as thermoelectric applications. Investigations on chalcogenide perovskites such as $CaHfS_3$ in the orthorhombic phase, carried out by Kassa et al. [8], revealed dynamic stability, ductility, and positive optoelectronic properties. The findings highlight the diverse functional potential of perovskites and demonstrate the importance of first-principles approaches in guiding materials discovery. Khan et al. [17] examined $HfXO_3$ (X = Be, Mg) perovskites, confirming structural stability through the Birch–Murnaghan equation of state. Their results revealed indirect narrow band gaps of 1.14 eV for $HfBeO_3$ and 0.8 eV for $HfMgO_3$, alongside pronounced elastic anisotropy. Husain et al. [18] investigated $BaAgF_3$ and $BaCuF_3$ ternary halide perovskites, identifying them as thermodynamically and mechanically stable, with indirect narrow band gaps of 0.2 eV and 0.3 eV, respectively. The results suggest their suitability for UV devices and thermoelectric energy harvesting. Further studies by Saddique et al. [19] on $GaBaF_3$ and $InBaF_3$ cubic fluoroperovskites confirmed mechanical stability, ductility, and resistance to plastic deformation. With direct wide band gaps of 5.0 eV and 5.1 eV, these compounds are promising for UV optoelectronic applications. Moreover, Khera et al. [20] investigated $BaXO_3$ (X = Hf, Ti, V) for solar cell applications, identifying $BaTiO_3$ as the most promising candidate due to its thermoelectric efficiency and strong light absorption, while $BaVO_3$ was recognized for its pronounced UV absorption linked to high electronegativity. Sadiq et al. investigated the properties of Rb_2InGeX_6 (X = Cl, Br, I) and revealed tunable semiconducting to semi-metallic performance with promising thermoelectric and optoelectronic features, highlighting their suitability for next-generation PV and energy-harvesting applications [21]. Abdulla et al. studies the DFT-based study on Rb_2AgSnX_6 (X = Cl, Br, I) double perovskites and confirmed their structural stability and metallic nature, together with remarkable optical transparency and light–matter interaction properties, suggesting their potential for transparent conductors and advanced photonic devices [22].

Recent first-principles investigations have highlighted the growing importance of chalcogenide, MAX-phase, oxide, and halide perovskite materials for advanced optoelectronic, PVs, thermoelectric, magnetic, and spintronic applications. Studies on Cu_2CdMSe_4 (M = Zr, Hf) by Fatima et al. revealed promising semiconducting behaviours, high optical absorption, and capable thermoelectric performance, indicating their suitability for solar energy conversion and optoelectronic devices [23]. Likewise, Ti_3AC_2 (A = P, As, Cd) MAX compounds by Khalil et al. exhibited excellent mechanical stability, hardness, and conductive characteristics, making them potential candidates for coating and electronic applications [24]. Yaqoob et al. demonstrated remarkable magnetic and transport properties of half-metallic $AMnTe_2$ (A = Li, Na, K) and KXO_2 (X = Pr, Nd, Pm) compounds with strong spin polarization, highlighting their potential for spintronic technologies [25]. Furthermore, Fatima et al. studied novel chalcogenides MAg_3Se_4 (M = V, Nb, Ta) and showed excellent structural stability, suitable band gaps, ductile nature, and attractive optical response for photovoltaic applications [26]. In parallel, Pb-free double halide perovskites such as, Cs_2SiBr_6, Cs_2GeBr_6, Cs_2SnBr_6, and Cs_2CaSnX_6 (X = Cl, Br, I) were reported to possess electronic band gaps, high optical absorption, mechanical stability, and thermodynamic robustness, confirming their promise for next-generation photovoltaic, optoelectronic, and resistive memory devices [27–29]. In oxide perovskites, Siddique et al. [30] employed SCAN and TB-mBJ functionals to investigate $BaHfO_3$ and $SrHfO_3$, achieving excellent agreement with experimental data and improved band gap predictions at a reduced computational cost relative to hybrid DFT methods. Furthermore, Rahman et al. [7] studied $CaZrS_3$ and $BaZrS_3$ chalcogenide perovskites, confirming direct band gap semiconducting performance and identifying them as attractive candidates for solar absorbers, optoelectronics, and thermal barrier coatings. Despite considerable advancements in the investigation of oxide, halide, and chalcogenide perovskites, thorough research on $BaHfS_3$ is still inadequate. The interaction of finite-temperature structural stability, electronic transport, and optical response has not been extensively examined. This research addresses the gap by using DFT alongside AIMD to provide a comprehensive evaluation of the structural, elastic, electronic, optical, and thermoelectric properties of $BaHfS_3$, thereby confirming its potential as a multifunctional material for advanced optoelectronic and thermoelectric applications.

2. Computational methodology

First-principles calculations were carried out using DFT as implemented in the *Quantum ESPRESSO* (QE) package [31,32]. The plane-wave pseudopotential formalism was adopted under full periodic boundary conditions. Exchange–correlation (*XC*) effects were treated using the generalized gradient approximation (GGA) within the Perdew–Burke–Ernzerhof (*PBE*) parameterization [33]. Norm-conserving pseudopotentials were selected for Ba, Hf, and S to ensure an accurate representation of valence–core interactions. A plane-wave kinetic-energy cutoff of 1360 eV and a charge-density Cutoff of 1.0884×10^4 eV were applied after regular convergence testing of total energy and electronic structure. Brillouin-zone (*BZ*) sampling employed a $10 \times 10 \times 10$ Monkhorst–Pack k-point mesh [34] for structural optimization, while a denser $12 \times 12 \times 12$ mesh was used for DOS calculations to better resolve near-edge features. Structural relaxation proceeded until the Hellmann–Feynman forces on all atoms were reduced below 0.0014 eV/atom, and total-energy (E_T) convergence was achieved with an accuracy better than 10^{-6} Ry.

In this work, the cubic phase of $BaHfS_3$ was modelled using the ideal perovskite symmetry, which crystallizes in the $Pm-3m$ space group (*No*. 221). In this high-symmetry configuration, the Ba atom occupies the A-site Wyckoff position at (0,0,0), while the Hf atom is located at the B-site position (0.5, 0.5, 0.5). The three S atoms reside at the face-centered X-site positions (0.5, 0.5, 0), (0.5, 0, 0.5), and (0, 0.5, 0.5), forming the ideal BX_6 octahedral framework. The ideal cubic phase structure of the perovskite is shown in Fig. 1a. Although $BaHfS_3$ typically stabilizes in lower-symmetry orthorhombic structures under ambient conditions, the cubic $Pm-3m$ phase is frequently employed in first-principles simulations to investigate idealized structural, electronic, optical, and high-temperature properties. Electronic band structures were computed along high-symmetry paths of the *BZ* and explained in 3.3 section. TDOS and PDOS were obtained using self-consistent charge densities followed by non-self-consistent calculations on enhanced k-point sampling. Optical properties were evaluated within DFPT [35], assuming the independent-particle approximation. Both the real and imaginary parts of the frequency-dependent dielectric constants, $\varepsilon(\omega) = \varepsilon_1(\omega) + i\varepsilon_2(\omega)$, were calculated over the 0 – 30 eV photon-energy range, enabling the extraction of key optical quantities, such as the absorption coefficient $\alpha(\omega)$, extinction coefficient $\kappa(\omega)$, reflectivity (R), refractive index $n(\omega)$, and energy-loss spectrum $L(\omega)$. Thermoelectric properties

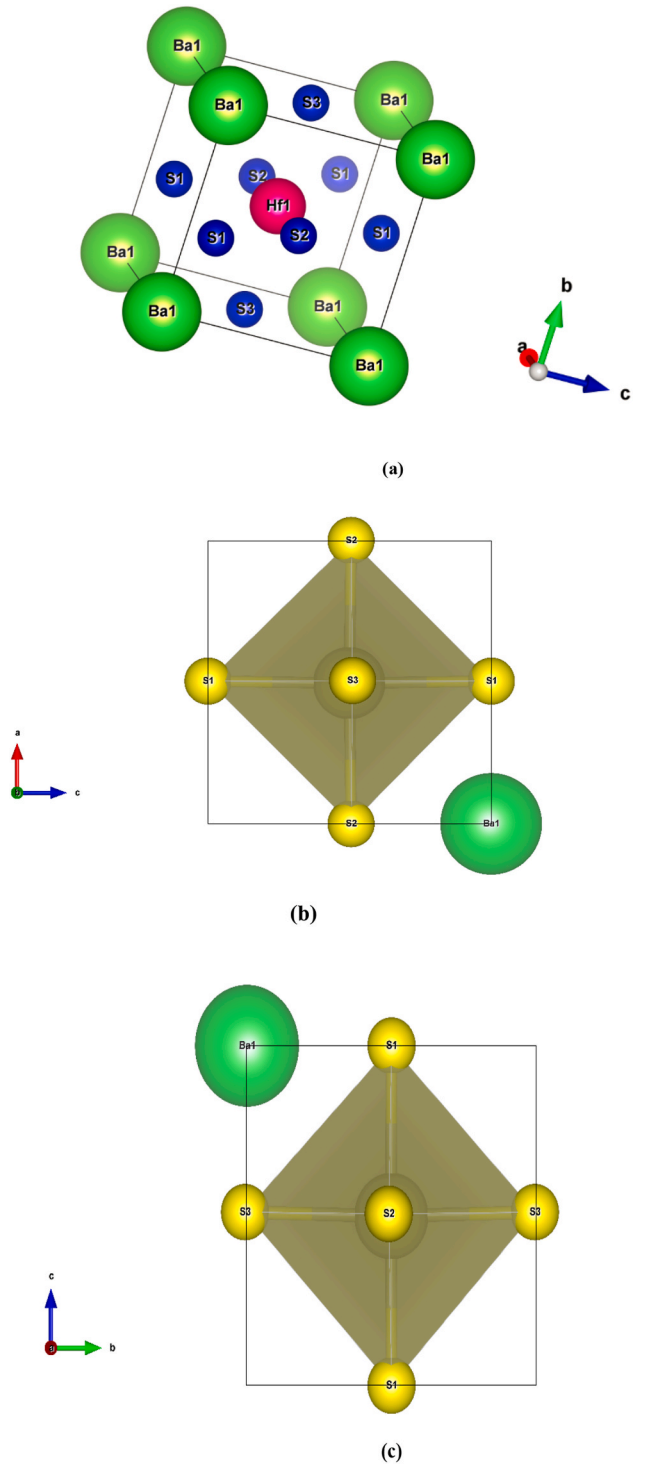


Fig. 1. The visualised structure of $BaHfS_3$ a) ideal cubic phase structure of $BaHfS_3$ b, c) The crystal framework of $BaHfS_3$.

were computed using the semi-classical BTT as implemented in *BoltzTraP* [36,37]. Non-self-consistent field (*NSCF*) calculations on a 24× 24 × 24 k-point mesh was used for Fourier interpolation of band energies. Transport coefficients, including the *S*, (σ/τ), electronic thermal conductivity (κ_e/τ), Hall coefficient (R_H), and carrier concentration were evaluated within the constant relaxation-time approximation (*CRTA*) over the 100–1000 K temperature range. Finally, finite-temperature dynamical stability was assessed using AIMD simulations performed in the canonical ensemble (NVT). A Nosé–Hoover thermostat-maintained temperature stability during the 1800 fs simulation with a 1 fs time step, enabling identification of structural robustness and thermal fluctuations of the *Pm-3m* phase.

3. Results and discussion

3.1. Structural properties

The structural characteristics of the $BaHfS_3$ chalcogenide perovskite were optimized using DFT, and the resulting parameters are summarized in Table 1. The crystal structure, illustrated in Fig. 1, adopts the perovskite-type framework in the *Pm-3m* space group, consisting of corner-sharing HfS_6 octahedra with Ba occupying the interstitial A-site positions. The Goldschmidt tolerance factor (*t*), calculated from the ionic radii of Ba, Hf, and S, is approximately 0.93, a value consistent with the stabilization of distorted perovskite phases. This deviation from unity indicates that $BaHfS_3$ naturally octahedral tilting as a mechanism for minimizing internal structural strain. The structural stability of perovskites is commonly assessed using the (t), expressed as [38]:

$$t_G = \frac{(r_{Rb} + r_X)}{\sqrt{2}(r_B + r_X)} \quad (1)$$

where r_{RB}, r_B, and r_X denote the ionic radii of Ba, Hf, and S, respectively. For $BaHfS_3$, the calculated tolerance factor of approximately **0.93** confirms the stability of the distorted phase ($Pm-3m$ *symmetry*), consistent with typical values for chalcogenide perovskites.

The octahedral distortion parameter (0.38587) further substantiates a significant divergence from ideal octahedral symmetry. These distortions are essential for stabilizing the *Pm-3m* phase and structuring the electronic structure of the material, affecting band dispersion, orbital hybridization, and carrier transport. The bond lengths at the three distinct S sites (≈2.48–2.52 Å) display minor variations, highlighting the anisotropic coordination surrounding Hf and the existence of non-uniform crystal fields characteristic of chalcogenide perovskites. Octahedral tilting affects the interaction between *Hf-d* states and *S p* states, which directly determines the bandgap magnitude and carrier mobility. The computed *t* of $BaHfS_3$ is consistent with other stable ABX_3 sulfide perovskites, such as $BaZrS_3$ or $SrHfS_3$ [39].

$BaHfS_3$ demonstrates robust thermodynamic stability, evidenced by its markedly negative E_f (−6.67 eV) and E_T (−18122.3 Ry). The results jointly affirm that the optimized structure is both physically plausible and energetically advantageous, establishing a robust basis for ensuing electronic, optical, and thermoelectric studies. Fig. 1b and c shows the *Pm-3m* structure of $BaHfS_3$, wherein corner-connected HfS_6 octahedra create a three-dimensional framework, with Ba atoms situated in interstitial positions. The observable octahedral tilting pattern is indicative of deformed perovskites and corresponds to a tolerance factor less than one. This visual verification supports the quantitative structural parameters presented in Table 1, affirming the stability of the stricture phase. The unique octahedral tilting pattern linked to the *Pm-3m*

Table 1
The computed structural parameters of the investigated structure $BaHfS_3$.

Calculated structural parameters			
Total Energy (Ry)			−18122.3
Lattice Constant (Å)			4.9958
Formation Energy (eV)			−6.67496
Volume ($Å^3$)			124.6866
Tolerance Factor			0.932095
Octahedral Distortion			0.38587
Bonds length (Å)			
S1-Ha-S1	2.50612	2.4902	4.99632
S2-Ha-S2	2.51671	2.48032	4.99703
S3-Ha-S3	2.52159	2.47645	4.99804

perovskite family, visually corroborating the structural characteristics derived from DFT optimization is illustrated in Fig. 1.

The calculated energy–volume (E–V) relationship of the $BaHfS_3$ chalcogenide perovskite is demonstrated in Fig. 2. The relationship shows the characteristic parabolic behaviour of a thermodynamically stable crystalline structure and confirms the existence of a well-defined equilibrium state. As the unit-cell volume approaches the equilibrium value of approximately 124.69 $Å^3$, the E_T gradually decreases and reaches a minimum value near -2.46566×10^5 eV, indicating the most promising configuration of the investigated structure. The smooth and symmetric increase in total energy on both sides of the equilibrium point demonstrates that both lattice compression and expansion result in energetically negative states because of enhanced interatomic repulsion and weakened bonding interactions, respectively. The presence of a distinct global minimum further confirms the structural stability of the optimized Pm-3m phase and validates the reliability of the obtained lattice parameters for subsequent electronic, optical, elastic, and thermodynamic investigations.

The *AIMD* simulation depicted in Fig. 3 demonstrates negligible variations in E_T over 1800 fs, exhibiting neither rapid shifts nor indications of phase transitions. The moderate oscillations result from anticipated thermal vibrations of atoms near their equilibrium positions, affirming that $BaHfS_3$ maintains dynamic stability at the simulated temperature. The lack of structural failure or uncontrolled energy dynamics clearly indicates that the *Pm-3m* phase of $BaHfS_3$ is resilient to thermal disturbances. This result is significant as dynamic stability enhances thermodynamic stability (derived from E_f) and bolsters trust in $BaHfS_3$ as a dependable contender for optoelectronic and thermoelectric applications. After confirming the thermodynamic and geometric stability of $BaHfS_3$, it is necessary to assess the impact of its atomic configuration and octahedral distortions on its mechanical properties. As a consequence, the elastic constants and directional mechanical properties are analyzed to correlate structural deformations with macroscopic stability.

3.2. Elastic anisotropy: 3D polar surfaces

The structural stability of $BaHfS_3$ is primarily determined by its tolerance factor and the extent of octahedral distortion in the HfS_6 framework. A tolerance factor near unity fosters a stable perovskite structure, whereas deviations result in rotations and tilts of the octahedra, thus affecting the bonding geometry and mechanical performance. The moderate octahedral tilting in $BaHfS_3$, associated with *Pm-3m* symmetry, results in direction-dependent stiffness and enhances the structure's anisotropic characteristics. Table 2 consolidates the computed elastic constants and resultant mechanical moduli of $BaHfS_3$.

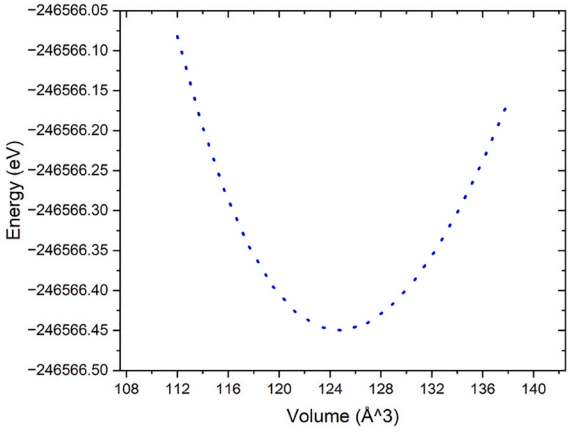


Fig. 2. The energy–volume (E–V) relationship of the $BaHfS_3$ chalcogenide perovskite.

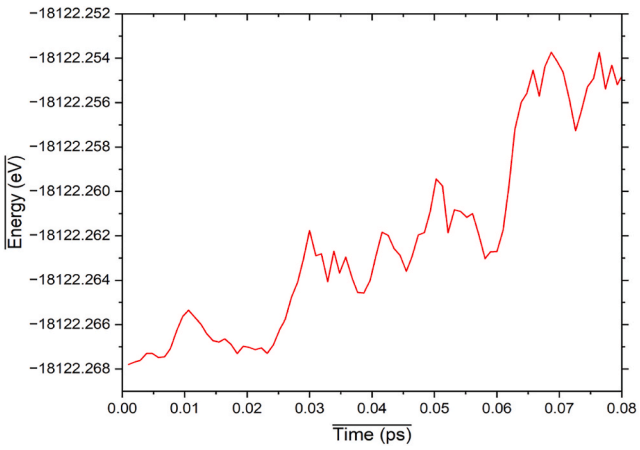


Fig. 3. Energy fluctuations of $BaHfS_3$ as a function of simulation time (fs) from AIMD simulations.

Table 2
The calculated elastic constants and derived moduli of $BaHfS_3$ in GPa.

Computed parameters	Obtained results in (GPa)
Bulk modulus (B)	76.53026
Young modulus (E)	109.0173
Shear modulus (G)	43.17834
Poisson Ratio (υ)	0.26241
C_{11}	154.1417
C_{12}	37.72456
C_{44}	35.29857
C_{11}-C_{12}	116.4171
C_{11}+2C_{12}	229.5908
Cauchy pressure (σ)	118.8431
Pugh's ratio (B/G)	1.772423

The bulk modulus (B = 76.53 GPa) signifies that $BaHfS_3$ exhibits moderate resistance to uniform compression, in accordance with the rather open structure of its chalcogenide perovskite lattice. The Young's modulus (E = 109.02 GPa) further substantiates that the material is mechanically robust although not very rigid, aligning with expectations for compounds exhibiting substantial octahedral tilting and mixed ionic-covalent bonding. The stable energy profile indicates the thermodynamic and dynamic stability of the *Pm-3m* phase.

The shear modulus (G = 43.18 GPa) is significantly lower than the (E), indicating the facility of angular distortion inside the HfS_6 network. This phenomenon is characteristic of perovskites, wherein the rotational degrees of freedom surrounding the octahedra diminish the shear response. The Poisson ratio (ν = 0.262) positions $BaHfS_3$ within the standard range for inorganic solids, signifying a harmonious balance of ductility and brittleness.

The various elastic constants (C_{11}, C_{12}, C_{44}) exhibit the anticipated hierarchy for a perovskite, with C_{11} (154.14 GPa) obviously exceeding C_{12} (37.72 GPa) and C_{44} (35.30 GPa). The significant value of $C_{11}-C_{12}$ (116.42 GPa) corroborates robust resistance to uniaxial deformation along the most rigid crystallographic axis. Simultaneously, the combination $C_{11} + 2C_{12}$ offers additional evidence of moderate overall compressibility. From a mechanical stability and adhesion standpoint, the Cauchy pressure (σ = 118.84 GPa) is positive and elevated. This outcome indicates a prevailing metallic or ionic bonding nature with significant core interatomic forces, in alignment with *Ba–S* and *Hf–S* interactions. The Pugh's ratio (B/G = 1.77) somewhat undercuts the ductile–brittle threshold of 1.75–2.00, situating $BaHfS_3$ in the borderline category, albeit inclined towards brittle performance. This corresponds effectively with the reported anisotropic elastic surfaces; wherein specific orientations exhibit elevated stiffness and constrained plastic deformation.

The elastic response of the chalcogenide perovskite $BaHfS_3$ were investigated by first-principles calculations to comprehend the orientation-dependent mechanical manner. Fig. 4 describes the three-dimensional (3D) polar distributions of the primary elastic moduli: E (Fig. 4a), G (Fig. 4b), and $\nu(\hat{n})$ (Fig. 4c) across all crystallographic orientations. In an isotropic solid, these surfaces would be entirely spherical. The protrusions and depressions seen in $BaHfS_3$ affirm its significant elastic anisotropy, stemming from the $Pm-3m$ structure and the irregular connectivity of the Ba–S interactions and HfS_6 octahedra

E has peak values at the [100] and [010] orientations, where the octahedral framework is most densely interconnected. In contrast, the [001] direction demonstrates significantly reduced stiffness, indicating a rather flexible axis. This mechanical softness indicates diminished cross-linking and more flexibility in tilting modes in that orientation. An analogous anisotropic pattern manifests in the shear modulus surface, exhibiting distinct lobes that partially correspond with those of E. This overlap signifies that orientations opposing axial deformation also tend to counteract shear. Nevertheless, the minor angular displacement of the shear lobes indicates that shear deformation engages distinct bonding environments compared to uniaxial tension, especially in intermediate directions like [011].

$\nu(\hat{n})$, consistently ranging from 0.15 to 0.35 across all orientations, affirms mechanically stable performance. The directional surface is stretched along the axis of minimal stiffness in the [001] direction, indicating that lateral strains are most pronounced when axial loading is applied along this softer crystallographic axis. In contrast, limited lateral

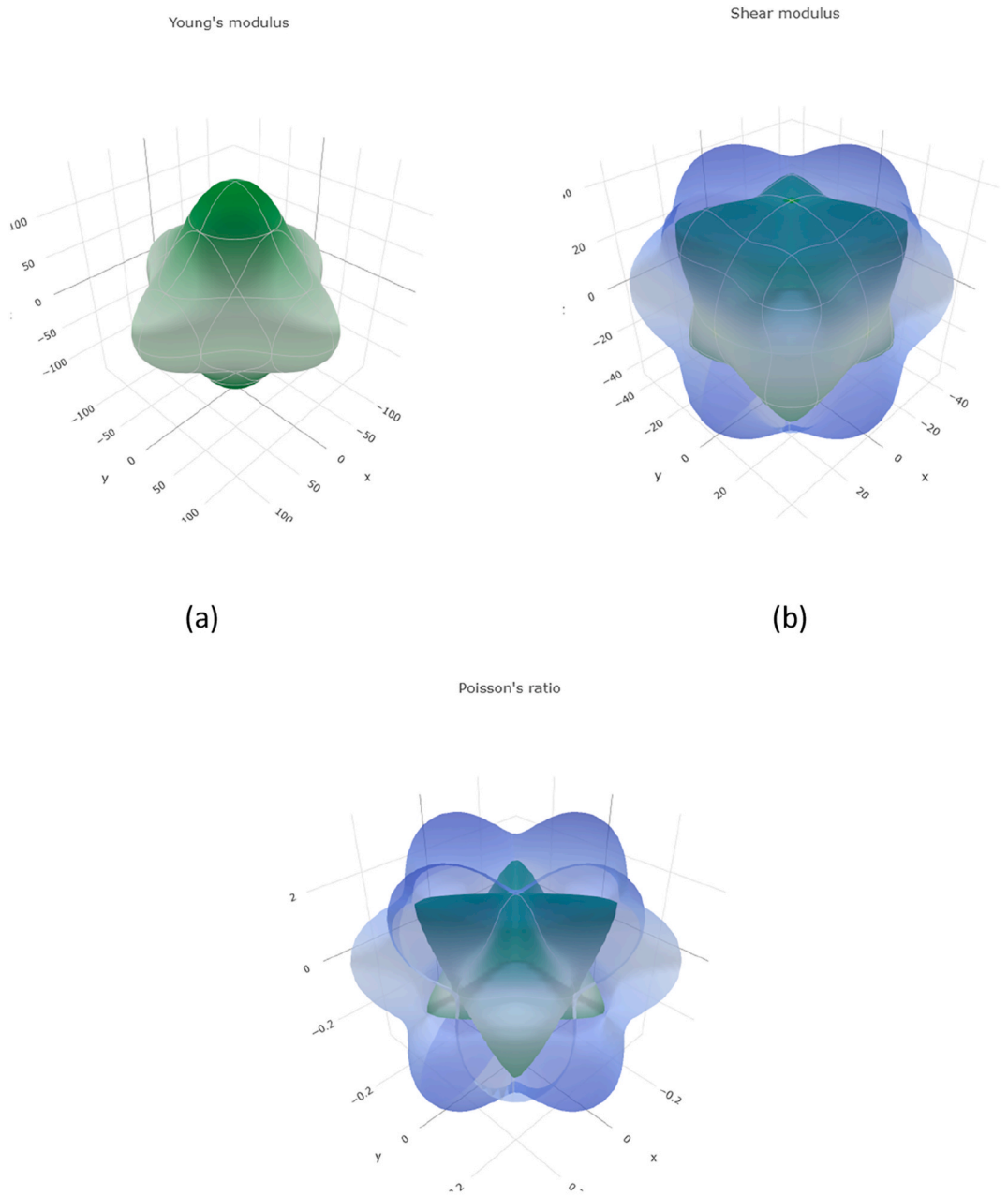


Fig. 4. 3D polar representations of the directional elastic response of $BaHfS_3$ (Pm-$3m$). (a) Young's modulus $Y(\hat{n})$, (b) shear modulus $G(\hat{n})$, and (c) Poisson's ratio $\nu(\hat{n})$.

displacement is projected for loading along the more rigid [100] and [010] axes. The intricate directional performance is crucial for forecasting crack initiation and propagation in polycrystalline $BaHfS_3$, where stress concentrations typically favor orientations with low stiffness or high $v(\hat{n})$. $Y(\hat{n})$ shows pronounced stiffness maxima along [100] and [010] and a minimum along [001], Fig. 1a. $G(\hat{n})$ indicates orientation-dependent resistance to shear and lobes that partially overlap those of E, Fig. 1b. $v(\hat{n})$ plotted as a transparent surface, with larger lateral contraction associated with loading along the softer [001] axis, Fig. 1c. Surfaces were generated from the computed elastic tensor and are plotted over all crystallographic orientations to emphasize the strong elastic anisotropy arising from the tilted HfS_6 octahedra.

The combined effect of a moderate *B* and a low *G* indicates that $BaHfS_3$ is more capable of withstanding compressive loads than shear stresses, a crucial factor for device construction or thermal-mechanical cycling. The pronounced anisotropy demonstrated by both Fig. 4 and the elastic constants implies that grain orientation would substantially affect mechanical reliability in polycrystalline samples, a finding that can inform materials processing and sintering methodologies. The substantial $\boldsymbol{\sigma}$ substantiates the assertion that $BaHfS_3$ mainly exhibits ionic bonding, aligning with its electronic structure and potentially affecting phonon scattering manner pertinent to thermoelectric applications. The borderline ductile and brittle features indicated by the $\boldsymbol{B}/\boldsymbol{G}$ are associated with cubic octahedral tilting, which imparts rigidity in certain directions while permitting moderate compliance in others, hence reinforcing the structural–mechanical correlation in the text. The significant elastic anisotropy and octahedral tilting identified in the mechanical investigation directly influence orbital overlap and band dispersion. Accordingly, understanding the electronic band structure and DOS (presented in the next section) is essential for linking mechanical deformation pathways to electronic transport performance.

3.3. Electronic properties

The electronic properties of $BaHfS_3$ are determined by a complex interaction of orbital hybridization, band-edge topology, and the effective masses of charge carriers. Comprehending these features is essential, as they directly affect charge transport, excitation dynamics, and the optical response of the material. In semiconducting perovskites like $BaHfS_3$, the nature and relative significance of orbital contributions around the Fermi level dictate the ease with which electrons and holes engage in conduction processes and the strength of their interactions with the crystal lattice. Fig. 5 represents the electronic band structure of $BaHfS_3$ along high-symmetry directions in the BZ, highlighting the indirect fundamental band gap of 0.7 eV (R→Γ) and TDOS and PDOS of the investigated perovskite structure, illustrating the contributions of Ba, Hf, and S orbitals to the electronic states. The band diagram indicates a clear semiconducting feature, defined by an indirect fundamental band gap of 0.7 eV that separates the valence band maximum (VBM) at the R point from the conduction band minimum (CBM) at the Γ point. The extrema at the VBM and CBM occur at distinct k-points, necessitating phonon involvement for electron excitation across the bandgap, hence affecting intrinsic conductivity and thermally stimulated carrier production. The indirect character of the gap imposes intrinsic constraints on low-energy electronic transitions.

An additional yet significant characteristic is the existence of a direct band-gap transition at the Γ point, where a marginally lower valence sub-band engages in a direct transition with the CBM. While this is not the intrinsic bandgap, the Γ-point transition is anticipated to considerably influence optical absorption, as direct transitions do not necessitate momentum conservation. This property is especially pertinent for applications related to infrared absorption and thermoelectric response. It is important to note that typical DFT calculations are recognized for underestimating band gaps; hence, the true gap is likely more than 0.7 eV. The PDOS elucidates the orbital origin of the electronic states at the Fermi level, as indicated by the red dashed line in Fig. 5. The *S-2p* orbitals predominate in the VB, particularly around the VBM, highlighting robust covalent *Hf–S* interactions. The CB edge is mostly determined by *Hf-4d* states, signifying that charge carriers elevated into the CBM are chiefly Hf-centered.

The significant hybridization between *S-2p* and *Hf-4d* orbitals at the band boundaries verifies the existence of robust chemical bonding interactions influencing the electronic dispersion. In contrast, Ba contributes insignificantly near the band gap, with its states positioned further within the VB or well above the conduction edge, thereby highlighting its predominantly structural and electrostatic function. The TDOS confirms the semiconducting nature, exhibiting a clear gap at the Fermi level and prominent peaks associated with localized states originating from flatter areas in the band structure. The band structure and DOS investigations elucidate the orbital interactions that account for the observed semiconducting features.

S-2p orbitals confine holes adjacent to the VBM, while *Hf-4d* orbitals facilitate more delocalized electron states near the CBM. The robust hybridization between *Hf-4d* and *S-2p* orbitals is intricately linked to the

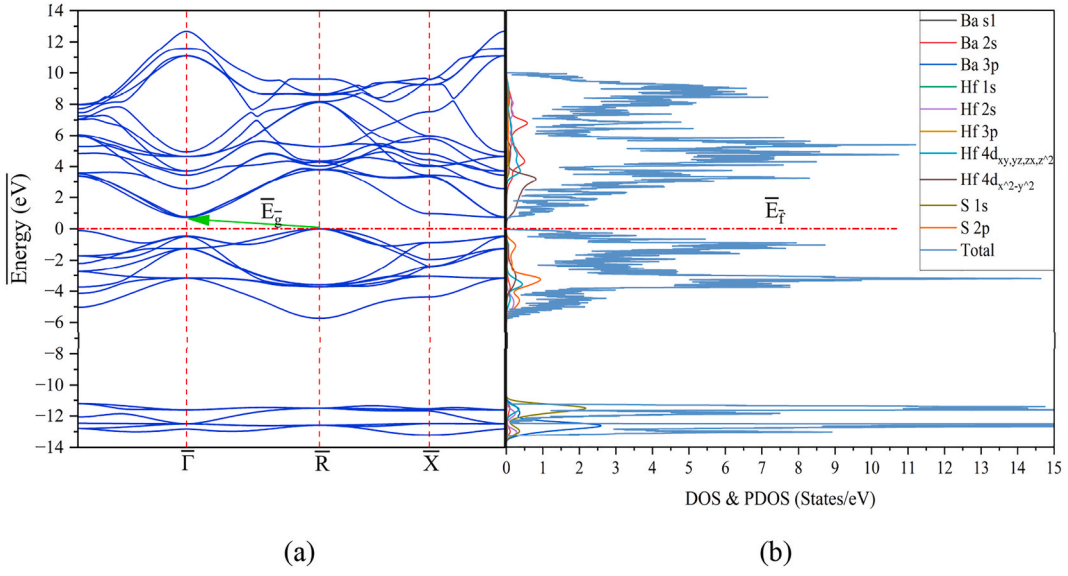


Fig. 5. Electronic structure of $BaHfS_3$. (a) Electronic band structure (b) DOS, PDOS and TDOS.

octahedral connectivity inside the perovskite framework, affecting effective mass anisotropy. The low m_e^* indicates its appropriateness for electrical and thermoelectric applications that need electron-dominated transport. Despite being indirect, $BaHfS_3$ has direct optical transitions at low energy, which may be advantageous for infrared (IR) optoelectronics. All redundant explanations regarding valence or conduction orbital contributions and the underestimate in DFT have been synthesized into succinct sentences.

The computed parameters in Table 3 are essential in the evaluation of carrier mobility and overall transport action. The band-gap values presented in Table 3 validate the semiconducting characteristics of $BaHfS_3$, in accordance with the DOS and band-structure analysis. The indirect band-gap nature indicates that electronic excitation across the gap is less efficient compared to direct-gap semiconductors; yet, the existence of a nearby competitive direct transition ensures that $BaHfS_3$ can nevertheless exhibit significant optical activity. The effective masses of carriers offer additional understanding of transport qualities. A reduced m_e^* signifies enhanced band dispersion around the CBM, implying that electrons can more readily react to external forces and hence exhibit greater mobility. On the other hand, a greater m_h^* indicates flatter VBs, which predicts more concentrated hole states with diminished mobility.

This electron–hole mass imbalance is characteristic of transition-metal chalcogenides, wherein CBs originating from d-orbitals exhibit greater dispersion than VBs obtained from p-orbitals. From a materials-design standpoint, the effective-mass values in Table 3 suggest that electron transport will possibly prevail over hole transport, aligning with the PDOS results indicating that the CB is predominantly produced from *Hf-4d* states. Reduced m_e^* enhance thermoelectric performance by improving carrier mobility while minimally diminishing the *S*. Table 3 substantiates the assertion that $BaHfS_3$ is an indirect yet transport-efficient semiconductor with advantageous electron conduction properties. The computed findings enhance the PDOS study and create a cohesive understanding of how orbital contributions and band topology together govern the electrical performance of the investigated perovskite structure. The electronic band topology governs permitted optical transitions and influences the interaction between photons and charge carriers, therefore providing a basis for examining the optical response of $BaHfS_3$. As a consequence, the optical properties are analyzed in the next section to assess the appropriateness of the structure for light-harvesting and photonic applications.

The electronic band gap of the investigated perovskite structure was further evaluated using advanced *XC* approaches beyond standard DFT. While conventional GGA-based functionals are known to underestimate band gaps because of the absence of derivative discontinuity, in this work the hybrid Heyd–Scuseria–Ernzerhof (HSE) functional and many-body perturbation theory within the Green Function (GW) approximation were employed for purposes of obtaining a more reliable approximation of the quasiparticle band gap. As reported in Table 3, the HSE functional obtain a prominently larger value of band-gap compared to GGA, reflecting the partial inclusion of exact Hartree–Fock exchange (HF), which improves the description of exchange interactions and electronic localization. In addition, the GW-calculated band gap shows an additional increase, as expected from the explicit treatment of electron–electron interactions and self-energy corrections. The progressive widening of the band gap from GGA to HSE and lastly to GW confirms the semiconducting nature of the studied perovskite and emphasizes the significance of many-body effects in precisely describing its electronic structure.

Table 3
The calculated minimum band-gap energy in (eV) and the effective masses of electrons m_e^* and holes m_h^* in $BaHfS_3$.

Compound	E_g^{GGA}	E_g^{HSE}	E_g^{GW}	m_e^*	m_h^*
$BaHfS_3$	0.7	1.3	1.6	−1.3564	0.4328

3.4. Optical properties

Comprehending the optical response of $BaHfS_3$ is fundamental for assessing its applicability in contemporary optoelectronic technologies, since these characteristics dictate photon absorption, dielectric screening, and light-matter interaction at the atomic level. The interaction between its electronic band structure and orbital hybridization significantly affects the initiation of optical transitions, facilitating the identification of spectrum regions pertinent to device integration. An in-depth examination of absorption features, dielectric functions, and energy-dependent responses offers essential insights into the applicability of the material in PV, photodetection, and photonic domains. A thorough computational analysis of the optical properties of $BaHfS_3$ is illustrated in Fig. 6. The $\alpha(w)$ in Fig. 6(a) is nearly nil below the fundamental band gap, indicating a lack of electronic transitions in this area. Beyond the band gap, absorption increases significantly, indicating the initiation of robust inter-band transitions from the VB to the CB. The $\kappa(w)$ described in Fig. 6b exhibits a comparable trend: it remains minimal at low photon energies, but accelerates at elevated energies, corroborating increased attenuation resulting from active electronic transitions.

The real part of the dielectric function, illustrated in Fig. 6c, exhibits a substantial static dielectric value at zero frequency, indicating a pronounced polarization response typical of materials with considerable ionic and electronic contributions. A decrease into negative values near ~2 eV indicates a potential plasmonic manner, which might be utilized for optoelectronic or photonic applications necessitating improved light confinement or dielectric tunability. As photon energy surpasses the band gap, the real dielectric response decreases, aligning with diminished polarization capacity at elevated excitation energies [40,41]. The imaginary dielectric function depicted in Fig. 6d displays significant peaks between 2 and 4 eV, associated with inter-band transitions predominantly involving hybridized *Hf-4d* and *S-3p* states. The clearly delineated characteristics highlight the promise of $BaHfS_3$ for use in visible-range photodetection, PV absorption, and high-k dielectric components.

To enhance the understanding of the interaction of $BaHfS_3$ with energetic photons and rapid electrons, supplementary optical metrics such as the energy loss function and *R* were assessed (Fig. 7). Fig. 7a illustrates the energy loss spectrum, featuring a significant peak near 21 eV, indicative of the bulk plasmon resonance, which represents collective oscillations of free electron density in reaction to external electromagnetic disturbances [42]. At lower energies (0–2 eV), the loss function is approximately zero, signifying negligible energy dissipation by rapidly moving electrons within this range. These plasmonic reactions are pertinent for radiation shielding, electron-beam apparatus, and high-energy photoelectronic interfaces. Fig. 7b illustrates the reflectance curve of $BaHfS_3$, commencing at around 0.4 in the low-energy infrared spectrum. This moderate *R* signifies a partial loss of incident photons resulting from surface reflections. As photon energy escalates, *R* it consistently diminishes, aligning with augmented absorption and the distinctive properties of semiconducting perovskites. A significant decrease in *R* above the plasmon resonance region signifies predominant bulk plasmon absorption, hence constraining radiative reflection at elevated energies. The persistence of the obtained *R* below unity across the studied range indicates the joint effects of inter-band absorption, dielectric losses, and inherent semiconducting properties, potentially influenced by structural characteristics or defect-mediated interactions.

Absorption coefficient demonstrates negligible absorption below the fundamental band gap followed by a rapid increase at around 2 eV associated with inter-band transitions. Extinction coefficient exhibits minimal attenuation at low energies and a pronounced rise with increasing photon energy. Real part of the dielectric function shows a

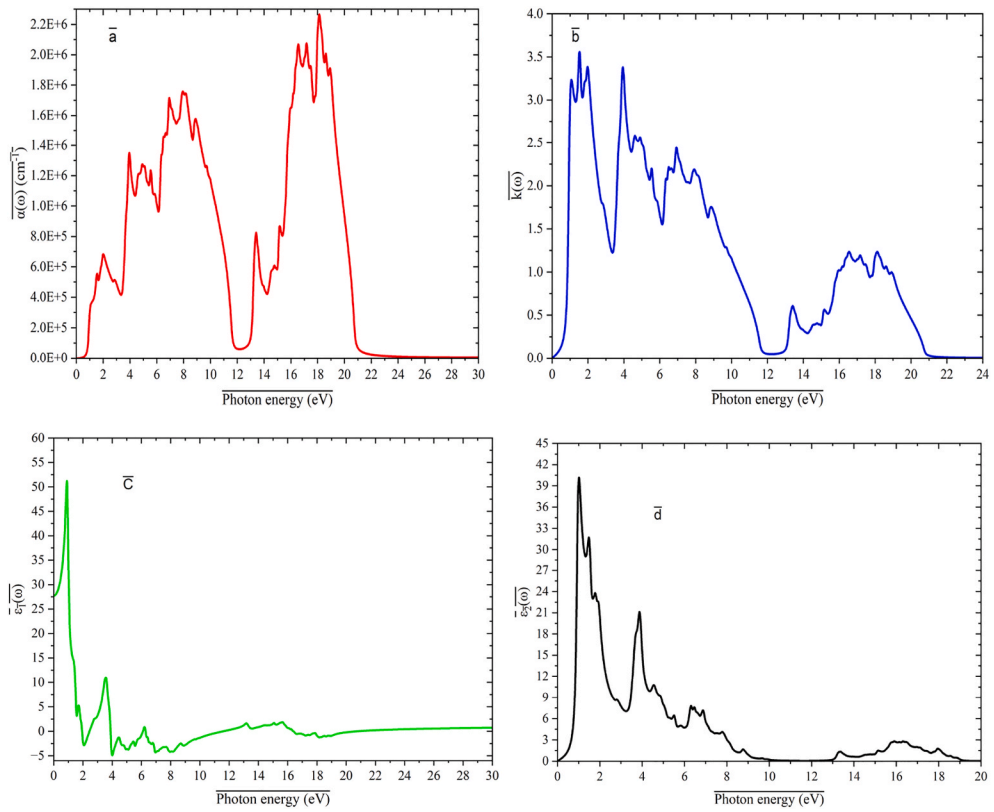


Fig. 6. Calculated optical properties of $BaHfS_3$ (a) Absorption coefficient, (b) Extinction coefficient, (c) Real part of the dielectric function. (d) Imaginary part of the dielectric function.

large static dielectric constant and a noted negative excursion near ~2 eV indicative of plasmonic action.

Imaginary part of the dielectric function highlights pronounced peaks from optically active transitions involving hybridized Hf–d and S–p states.

The refractive index of $BaHfS_3$, depicted in Fig. 7 (c), provides a deeper awareness of the photon-transport features of the material. At low photon energies, the refractive index demonstrates elevated values, signifying a pronounced ability to attenuate light, characteristic of semiconducting perovskites with significant dielectric polarization. It is noted from the figure that the n of the structure at zero frequency n (0) is 5.25 and increased to 7.25 at 1 eV. The refractive index profile of $BaHfS_3$ reveals a strong frequency-dependent optical response. The static refractive index of n (0) = 5.25 indicates a highly polarizable lattice in which both ionic and electronic contributions significantly enhance the low-frequency dielectric screening. As the photon energy increases, n rises to 7.25 at 1 eV, reflecting the commencement of strong dispersion associated with nearby interband electronic transitions. This enhancement demonstrates that the electronic states of $BaHfS_3$ interact more strongly with the incident radiation in the near-IR region, resulting in increased optical density and reduced light velocity within the material.

As the energy increases, the n regularity diminishes, illustrating dispersion dictated by electronic transition thresholds. Local fluctuations and tiny peaks correspond to the energies at which the imaginary dielectric function reaches maxima, validating that n variations stem from particular inter-band electronic excitations.

The amalgamation of these optical attributes-intense absorption near the band edge, plasmonic resonance at elevated energies, and a substantial static dielectric constant highlights the multifunctional optoelectronic potential of $BaHfS_3$. This strong visible-range absorption and unique dielectric properties of this compound make it a promising candidate for PV, light-harvesting technologies, photodetection devices, and applications necessitating adjustable refractive attitude, such as waveguides or optical modulators. Optical transitions and carrier dynamics additionally affect temperature-dependent transport phenomena, including heat capacity, electrical conductivity, and Seebeck response. Therefore, to finalize the physical description of the investigated chalcogenide perovskite structure, the thermodynamic and thermoelectric properties were evaluated in the next section to determine the performance of $BaHfS_3$ under practical operational sceneries.

3.5. *Thermodynamics properties*

Thermodynamic values reveal an essential comprehension of the temperature-dependent stability and transport characteristics of $BaHfS_3$, especially about its applicability in high-temperature thermoelectric applications. These properties regulate phonon activation, carrier production, and thermal transport mechanisms, therefore establishing the operating boundaries and overall efficiency of the material. A thorough comprehension of these characteristics enables us to relate microscopic structure dynamics to macroscopic functional performance.

Fig. 8 (a) illustrates the temperature-dependent characteristics of the (S), which rises consistently until around 300–400 K, then decreases at elevated temperatures. The bell-shaped curve, reaching around 0.305 mV/K around 350 K, delineates a temperature range where the interaction between carrier concentration and entropy per carrier is optimal for thermoelectric conversion. The constantly high S indicates p-type semiconducting nature, signifying that holes are the predominant charge carriers. The maximum Seebeck values correspond well with those documented for other high-performing chalcogenide perovskites, highlighting the viability of $BaHfS_3$ as a competitive thermoelectric material [43–45]. The post-peak degradation aligns with heightened intrinsic carrier concentration at elevated temperatures, which reduces the entropy contribution per carrier. Fig. 8 (b) demonstrates the σ/τ normalized by the square of the relaxation time (σ/τ^2), exhibiting an exponential increase with temperature, rising from almost zero at 200 K

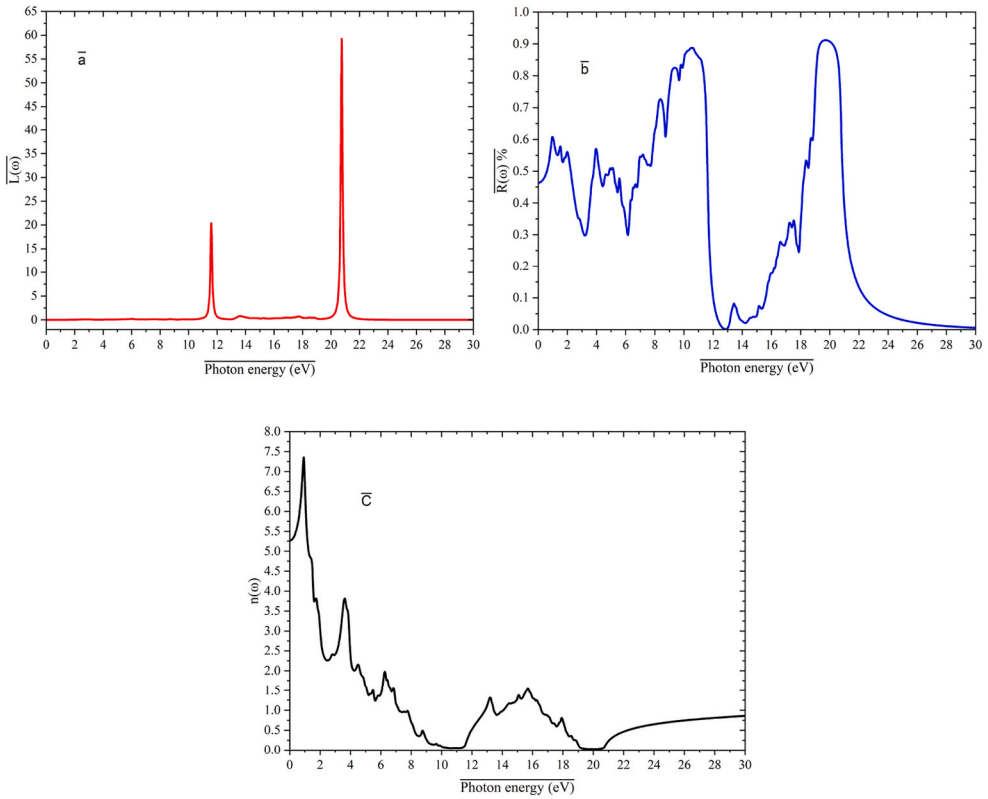


Fig. 7. Extended optical response of $BaHfS_3$ obtained from energy-dependent optical calculations. (a) Energy loss function, presenting a dominant plasmon resonance peak at ~21 eV and minimal losses below 2 eV. (b) Reflectivity spectrum, displaying moderate low-energy reflectance followed by a continuous decline and a sharp drop above the plasmonic region. (c) Refractive index profile as a function of photon energy, indicating strong dispersion manner and modifications near critical inter-band transition energies.

to approximately 4×10^{17} (Ω m. s) $^{-1}$ at 900 K. This pattern demonstrates standard semiconducting comportment influenced by thermally activated intrinsic carriers. At temperatures between 200 and 500 K, σ/τ stays low due to insufficient carrier excitation; however, a fast increase is observed beyond 500 K when electrons are elevated across the band gap, indicating Arrhenius-like carrier activation. This trend indicates that intrinsic carrier creation prevails over scattering at elevated temperatures, aligning with a band-gap-associated activation energy.

The R_H of the structure depicted in Fig. 8 (c) exhibits a pronounced decline with increasing temperature, decreasing from approximately 0.67×10^{-7} m^3/C at 300 K to roughly 0.015×10^{-7} m^3/C at 1000 K. The consistently positive R_H corroborates the p-type characteristics of $BaHfS_3$, aligning with the Seebeck analysis. The continuous reduction in R_H indicates a significant rise in carrier concentration with temperature, thus corroborating the conductivity trend in Fig. 8 (b). The swift rise in hole density elucidates the decline in S beyond 500 K, emphasizing the established inverse correlation between S and carrier concentration. The complimentary interaction among S, σ, and R_H highlights the semiconducting transport mechanism and confirms the internal consistency of the computed thermoelectric parameters [46].

Fig. 8 (d) displays the electronic thermal conductivity normalized by the square of the relaxation time (κ_e/τ^2), which exhibits a nonlinear increase from approximately 3×10^{13} W/(m. K·s) at 200 K to around 2.2×10^{14} W/(m. K·s) at 1000 K. The increase in κ_e, associated with σ via the Wiedemann–Franz relation, is predominantly ascribed to the temperature-driven augmentation in carrier concentration. The substantial atomic masses and intricate structures of Ba-, Hf-, and S-based perovskites are anticipated to diminish lattice thermal conductivity, a favorable attribute for attaining superior thermoelectric performance [41–43]. This indicates that $BaHfS_3$ may attain an advantageous equilibrium between elevated σ/τ and possibly reduced lattice thermal conductivity. Fig. 8 (e) indicates the temperature-dependent charge carrier concentration (N), which demonstrates a significant exponential increase from around zero at 200 K to around 3.5×10^{-2} at 1000 K. This pronounced temperature response is typical of intrinsic semiconductors, wherein thermal excitation produces both electrons in the CB and holes in the VB. The growing carrier population correlates with, and indeed elucidates, the significant increase in σ/τ^2 and the decline in R_H. As a result, carrier activation is the principal mechanism regulating the transport actions of $BaHfS_3$ at high temperatures. Fig. 8 (f) depicts the heat capacity at constant volume (C_V), increasing almost linearly from approximately 0.1 J/(mol· K) at 200 K to around 0.35 J/(mol. K) at 1000 K. This pattern signifies that more phonon modes are thermally filled as temperature rises, aligning with the anticipated features of crystalline materials nearing the Dulong–Petit limit at elevated temperatures. The rising coefficient of variation indicates improved anharmonic lattice interactions, which influence phonon scattering and may lead to a decrease in lattice thermal conductivity, a favorable attribute for thermoelectric applications. The consistent increase in C_V indicates strong structural integrity under thermal loading, crucial for device stability. The thermodynamic and transport analyses jointly highlight $BaHfS_3$ as a thermally stable, inherently p-type semiconductor with advantageous properties for high-temperature thermoelectric applications [47,48].

4. Conclusion

In this work, a first-principles investigation of cubic $BaHfS_3$ chalcogenide perovskite was performed by combining DFT, DFPT, BTT, and AIMD approaches to investigate its structural, mechanical, optoelectronic, and thermodynamic properties. Structural optimization confirmed the energetic stability of the Pm-3m phase through a

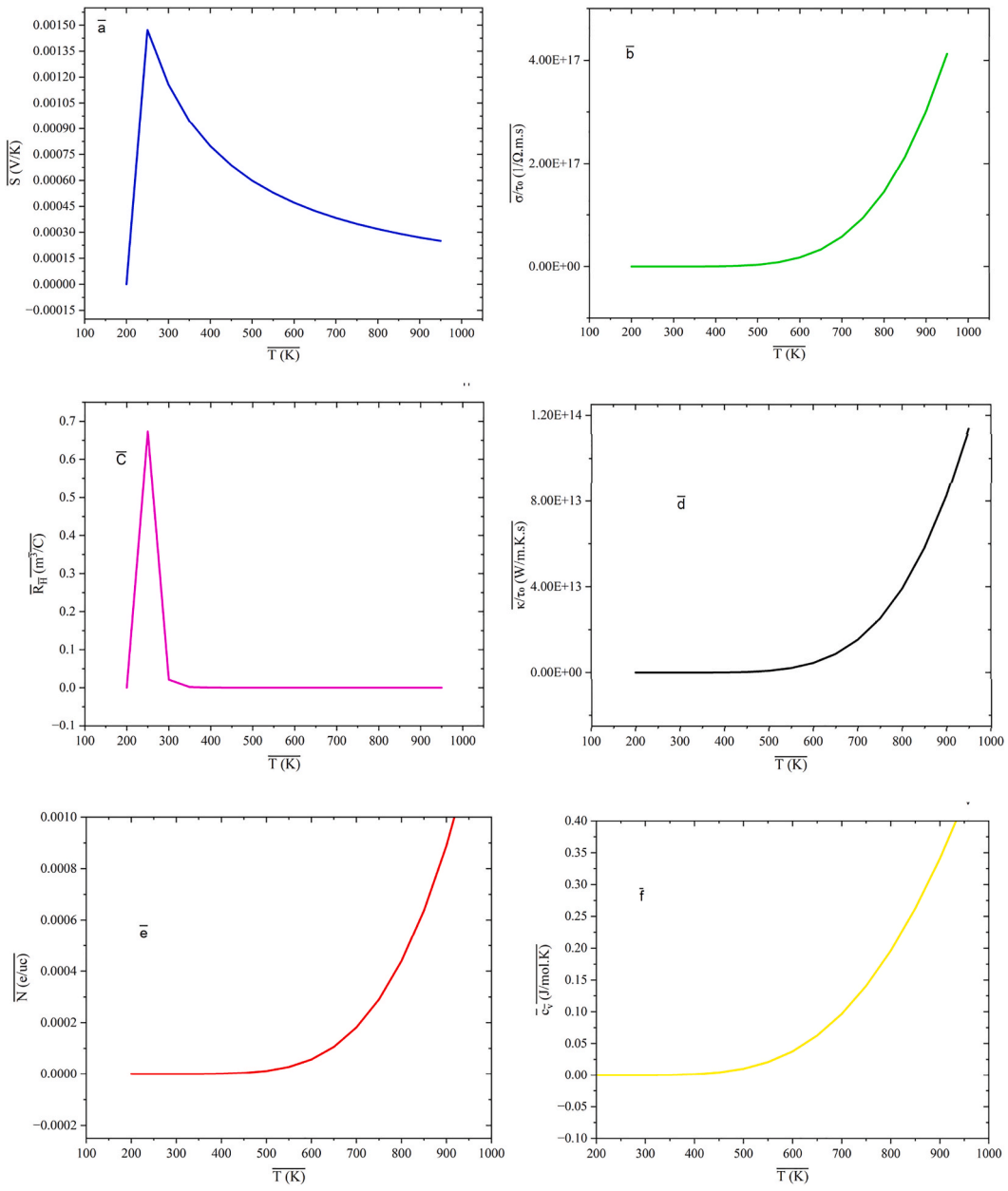


Fig. 8. Calculated temperature-dependent thermodynamics properties of $BaHfS_3$. (a) Seebeck coefficient (S) in mV/K. (b) Electrical conductivity in $(\Omega\ m.\ s)^{-1}$. (c) Hall coefficient (R_H) in m^3/C. (d) Electronic thermal conductivity in W/(m. K·s). (e) Charge carrier concentration (N). (f) Heat capacity at constant volume (C_V).

(t = 0.93), moderate octahedral distortion, and a negative E_f, indicating a stable perovskite structure. The AIMD analysis further demonstrated stable energy fluctuations under thermal conditions, confirming the dynamical robustness of the structure at finite temperatures. Mechanical calculations revealed that $BaHfS_3$ satisfies the stability criteria and exhibits pronounced elastic anisotropy arising from the distorted HfS_6 octahedral network. The calculated elastic moduli suggest moderate compressibility with a balanced mechanical response that combines structural rigidity with directional flexibility. Electronic structure analysis identified $BaHfS_3$ as an indirect semiconductor with a fundamental band gap of 0.7 eV, where the valence and conduction band edges are mainly governed by *S-2p* and *Hf-4d* orbitals, respectively. The lower electron effective mass relative to holes indicates carrier transport characteristics and enhanced electron mobility.

Optical investigations demonstrated strong absorption performance across the visible and UV regions with a high dielectric response, substantial refractive characteristics, and a distinct plasmon resonance feature. These properties suggest efficient light–matter interaction and indicate the suitability of $BaHfS_3$ for photonic and optoelectronic systems. Moreover, thermodynamic analyses revealed intrinsic p-type behaviours, high Seebeck response, increasing electrical conductivity with temperature, and good heat-capacity characteristics, highlighting its potential for thermal energy conversion at elevated temperatures. The integrated computational results establish $BaHfS_3$ as a thermally stable and multifunctional chalcogenide perovskite with promising electronic, optical, and transport features. The results of this research provide a theoretical basis for future experimental measurements and support the potential application of $BaHfS_3$ in next-generation optoelectronic and thermoelectric technologies.

CRediT authorship contribution statement

Nawzad A. Abdulkareem: Conceptualization, Data curation, Methodology, Supervision, Validation, Writing – review & editing.

Hameed T. Abdulla: Conceptualization, Validation, Visualization, Writing – original draft. **Diyar Sadiq:** Validation, Visualization, Writing – review & editing. **Mohammed Noor S. Rammoo:** Formal analysis, Investigation, Software. **Harun Akkus:** Project administration, Resources, Software, Supervision, Validation. **Mehmet Erzen:** Formal analysis, Investigation, Methodology, Resources, Software.

Declaration of competing interest

The authors declare that they have no known competing financial interests or personal relationships that could have appeared to influence the work reported in this paper.

Acknowledgement

The authors would like to thank the University of Zakho, College of Science, the Physics Department for their cooperation in completing this work.

Data availability

Data will be made available on request.

References

[1] M. Grätzel, The light and shade of perovskite solar cells, Nat. Mater. 13 (2014) 838–842.
[2] A.M. Ganose, C.N. Savory, D.O. Scanlon, Beyond methylammonium lead iodide: prospects for the emergent field of ns 2 containing solar absorbers, Chem. Commun. 53 (2017) 20–44.
[3] G. Kieslich, S. Sun, A.K. Cheetham, Solid-state principles applied to organic–inorganic perovskites: new tricks for an old dog, Chem. Sci. 5 (2014) 4712–4715.
[4] J. Even, L. Pedesseau, M.-A. Dupertuis, J.-M. Jancu, C. Katan, Electronic model for self-assembled hybrid organic/perovskite semiconductors: reverse band edge electronic states ordering and spin-orbit coupling, Phys. Rev. B Condens. Matter 86 (2012) 205301.
[5] R.E. Brandt, J.R. Poindexter, P. Gorai, R.C. Kurchin, R.L. Hoye, L. Nienhaus, M. W. Wilson, J.A. Polizzotti, R. Sereika, R. Zaltauskas, Searching for "defect-tolerant" photovoltaic materials: combined theoretical and experimental screening, Chem. Mater. 29 (2017) 4667–4674.
[6] S. Sun, T. Salim, N. Mathews, M. Duchamp, C. Boothroyd, G. Xing, T.C. Sum, Y. M. Lam, The origin of high efficiency in low-temperature solution-processable bilayer organometal halide hybrid solar cells, Energy Environ. Sci. 7 (2014) 399–407.
[7] M.Z. Rahman, S.S. Hasan, M.Z. Hasan, M. Rasheduzzaman, M.A. Rahman, M. M. Ali, A. Hossain, R.M. Khokan, M.M. Hossain, N.M. Mukhtar, Insight into the physical properties of the chalcogenide XZrS3 (X= Ca, Ba) perovskites: a first-principles computation, J. Electron. Mater. 53 (2024) 3775–3791.
[8] M. Kassa, N. Debelo, M. Woldemariam, Research Article the First-Principles Investigation of Structural Stability, Mechanical, Vibrational, Thermodynamic, and Optical Properties of CaHfS3 for Optoelectronic Application, 2023.
[9] J. Heyd, G.E. Scuseria, M. Ernzerhof, Hybrid functionals based on a screened Coulomb potential, J. Chem. Phys. 118 (2003) 8207–8215.
[10] F. Tran, P. Blaha, Accurate band gaps of semiconductors and insulators<? Format?> with a semilocal exchange-correlation potential, Phys. Rev. Lett. 102 (2009) 226401.
[11] S. Grimme, Density functional theory with London dispersion corrections, Wiley Interdiscip. Rev. Comput. Mol. Sci. 1 (2011) 211–228.
[12] D. Marx, J. Hutter, Ab Initio Molecular Dynamics: Basic Theory and Advanced Methods, Cambridge University Press, 2009.
[13] A. Katre, J. Carrete, N. Mingo, Unraveling the dominant phonon scattering mechanism in the thermoelectric compound ZrNiSn, J. Mater. Chem. A 4 (2016) 15940–15944.
[14] C. Carbogno, J. Behler, A. Groß, K. Reuter, Fingerprints for spin-selection rules in the interaction dynamics of O 2 at Al (111), Phys. Rev. Lett. 101 (2008) 096104.
[15] S.A. Khattak, M. Abohashrh, I. Ahmad, M. Husain, I. Ullah, S. Zulfiqar, G. Rooh, N. Rahman, G. Khan, T. Khan, Investigation of structural, mechanical, optoelectronic, and thermoelectric properties of BaXF3 (X= Co, Ir) fluoro-perovskites: promising materials for optoelectronic and thermoelectric applications, ACS Omega 8 (2023) 5274–5284.
[16] Q. Xia, Structural and elastic investigations of ternary perovskite BaMF3 (M= Ag, Cu) compounds. Experimental and Theoretical NANOTECHNOLOGY, 2023, pp. 283–290.
[17] S.N. Khan, A. Jehan, M. Husain, N. Rahman, V. Tirth, S.A. Shah, M. Uzair, M. Y. Khan, N. Sfina, M. Elhadi, Predicting structural, elastic, and optoelectronic properties of oxide perovskites HfXO3 (X= Be, Mg) employing the DFT approach, Optik 303 (2024) 171724.
[18] M. Husain, N. Rahman, R. Khan, M. Sohail, A.A. Khan, H.O. Elansary, T.K.Z. El-Abedin, E.A. Mahmoud, S.A. Abdelmohsen, A. Khan, Exploring the exemplary structural, electronic, optical, and elastic nature of inorganic ternary cubic XBaF3 (X= Al and Tl) employing the accurate TB-mBJ approach, Semicond. Sci. Technol. 37 (2022) 075004.
[19] J. Saddique, M. Husain, N. Rahman, R. Khan, A. Iqbal, M. Sohail, S.A. Khattak, S. N. Khan, A.A. Khan, A.H. Reshak, Modeling structural, elastic, electronic and optical properties of ternary cubic barium based fluoroperovskites MBaF3 (M= Ga and In) compounds based on DFT, Mater. Sci. Semicond. Process. 139 (2022) 106345.
[20] E.A. Khera, R. Ghodhbani, A. Nazir, H.M. Talha, I. Mukhtar, M. Manzoor, Y. Bakkour, R. Sharma, Quantum insights into physical characteristics for optoelectronic performance of TbSc1− xMxO3 (Mx= Cr, V; x= 0.25): a DFT approach, J. Electroceram. (2025) 1–11.
[21] D. Sadiq, N.A. Abdulkareem, H.T. Abdulla, M.N.S. Rammoo, Exploration of lead-free Rb2InGeX6 double perovskites: correlating halide substitution with electronic, optical, and thermoelectric performance, Physica Scripta 100 (2025) 095954.
[22] H.T. Abdulla, N.A. Abdulkareem, D. Sadiq, M.N.S. Rammoo, Metallic and optoelectronic properties of Rb2AgSnX6 (X= Cl, Br, I) double perovskites for photonic and transparent conductor applications: a DFT study, Int. J. Mod. Phys. B 40 (2026) 2650010.
[23] R. Fatima, R.A. Khalil, M.I. Hussain, First principles insight of Cu2CdMSe4 (M= Zr, Hf) quaternary chalcogenides as eco-friendly materials for optoelectronic and photovoltaic applications, Inorg. Chem. Commun. 174 (2025) 114031.
[24] R.A. Khalil, M.I. Hussain, N. Luqman, F. Hussain, A.M. Rana, M.S. Akhtar, R. F. Mehmood, DFT-based study of the structural, optoelectronic, mechanical and magnetic properties of Ti 3 AC 2 (A= P, As, Cd) for coating applications, RSC Adv. 12 (2022) 4395–4407.
[25] N. Yaqoob, B. Sabir, G. Murtaza, R.M.A. Khalil, N. Muhammad, A. Laref, Structural, electronic, magnetic, optical and thermoelectric response of half-metallic AMnTe2 (A= Li, Na, K): an ab-initio calculations, Phys. B Condens. Matter 574 (2019) 311656.
[26] R. Fatima, R.A. Khalil, M.I. Hussain, F. Hussain, Insight into the physical characteristics of novel inorganic chalcogenides MAg3Se4 (M= V, Nb, Ta) with exceptional stability using WIEN2K for its applications in photovoltaics, J. Indian Chem. Soc. 102 (2025) 101705.
[27] M.S. Hayat, R.A. Khalil, Computational predictions of optoelectronic energy materials Cs2SiBr6 Cs2GeBr6 & Cs2SnBr6 for phenomenal photovoltaic applications; a first principles study, Comput. Theor. Chem. 1235 (2024) 114532.
[28] S. Kiran, U. Mumtaz, A. Mustafa, M. Imran, F. Hussain, U. Rasheed, R. Khalil, E. A. Khera, A. Nazir, An ab initio investigation of the structural, mechanical, electronic, optical, and thermoelectric characteristics of novel double perovskite halides Cs 2 CaSnX 6 (X= Cl, Br, I) for optically influenced RRAM devices, RSC Adv. 13 (2023) 11192–11200.
[29] B. Tariq, G. Murtaza, H. Ali, S. Razzaq, R.A. Khalil, M.I. Hussain, K. Ismail, G. Nazir, N.H. Alotaibi, First principles study of the structural, half-metallic ferromagnetism, magnetic, and transport properties of KXO2 (X= Pr, Nd, and Pm) hexagonal oxides, Solid State Commun. 370 (2023) 115229.
[30] M.U. Siddique, U. Sardar, S. Tariq, A. Ali, DFT Study of Electronic and Magnetic Properties of SrHf0. 25Fe0. 75O3 and Defect-Driven Perovskites for Spintronics, Available at: SSRN 5415311, DOI.
[31] P. Giannozzi, O. Andreussi, T. Brumme, O. Bunau, M.B. Nardelli, M. Calandra, R. Car, C. Cavazzoni, D. Ceresoli, M. Cococcioni, Advanced capabilities for materials modelling with Quantum ESPRESSO, J. Phys. Condens. Matter 29 (2017) 465901.
[32] P. Giannozzi, O. Baseggio, P. Bonfà, D. Brunato, R. Car, I. Carnimeo, C. Cavazzoni, S. De Gironcoli, P. Delugas, F. Ferrari Ruffino, Quantum ESPRESSO toward the exascale, J. Chem. Phys. 152 (2020).
[33] J.P. Perdew, K. Burke, M. Ernzerhof, Generalized gradient approximation made simple, Phys. Rev. Lett. 77 (1996) 3865.
[34] H.J. Monkhorst, J.D. Pack, Special points for Brillouin-zone integrations, Phys. Rev. B 13 (1976) 5188.
[35] S. Baroni, S. De Gironcoli, A. Dal Corso, P. Giannozzi, Phonons and related crystal properties from density-functional perturbation theory, Rev. Mod. Phys. 73 (2001) 515.
[36] G.K. Madsen, D.J. Singh, BoltzTraP. A code for calculating band-structure dependent quantities, Comput. Phys. Commun. 175 (2006) 67–71.
[37] J.M. Ziman, Principles of the Theory of Solids, Cambridge university press, 1979.
[38] C.E. Tilley, Victor Moritz Goldschmidt 1888-1947, The Royal Society, London, 1948.
[39] A. Carr, T. Glinberg, N. Stull, J.R. Neilson, C.J. Bartel, Origins of chalcogenide perovskite instability, arXiv preprint arXiv:2506.11224 (2025).
[40] S.M. Samuel, S. Shaji, D.A. Avellaneda, B. Krishnan, Chalcogenide perovskites: enticing prospects across a wide range of compositions and optoelectronic properties for stable photodetector devices, Nano Express 6 (2025) 015002.
[41] E.K. Mahmoud, S. El-Dek, A.A. Farghali, M. Taha, Investigating the potential of triclinic ABSe3 (A= Li, Na, K, Rb, Cs; B= Si, Ge, Sn) perovskites as a new class of lead-free photovoltaic materials, Sci. Rep. 14 (2024) 22691.
[42] H.I. Eya, N.Y. Dzade, Density functional theory insights into the structural, electronic, optical, surface, and band alignment properties of BaZrS3 chalcogenide perovskite for photovoltaics, ACS Appl. Energy Mater. 6 (2023) 5729–5738.
[43] J.H. Al Shuhaib, J.F. Fernández, J. Bodega, J.R. Ares, I.J. Ferrer, F. Leardini, Synthesis, optical band gap and thermoelectric properties of Sr1+ xTiS3-y chalcogenide perovskites, Mater. Res. Bull. 167 (2023) 112405.

[44] X. Song, X. Shai, S. Deng, J. Wang, J. Li, X. Ma, X. Li, T. Wei, W. Ren, L. Gao, Anisotropic chalcogenide perovskite CaZrS3: a promising thermoelectric material, J. Phys. Chem. C 126 (2022) 11751–11760.
[45] Z. Yang, Y. Han, Y. Liang, W. Shen, Z. Zhang, C. Fang, Q. Wang, B. Wan, L. Chen, Y. Zhang, Chalcogenide perovskite BaZrS3 bulks for thermoelectric conversion with ultra-high carrier mobility and low thermal conductivity, Acta Mater. 276 (2024) 120156.
[46] X. Wang, V. Askarpour, J. Maassen, M. Lundstrom, On the calculation of Lorenz numbers for complex thermoelectric materials, J. Appl. Phys. 123 (2018).
[47] S. Wang, L. Zhang, Mechanical, optical, and thermoelectric properties of α-BaSnS 3 and β-BaSnS 3, RSC Adv. 15 (2025) 12179–12190.
[48] E. Osei-Agyemang, C.E. Adu, G. Balasubramanian, Ultralow lattice thermal conductivity of chalcogenide perovskite CaZrSe3 contributes to high thermoelectric figure of merit, npj Comput. Mater. 5 (2019) 116.